X-ray spectroscopic study of the chemical state of “invisible” Au in synthetic minerals in the Fe-As-S system

Trigub, A. L.; Tagirov, B. R.; Kvashnina, K. O.; Chareev, D. A.; Nickolsky, M. S.; Shiryaev, A. A.; Baranova, N. N.; Mokhov, E. V. Kovalchuk A. V.;

Originally published:

May 2017

American Mineralogist 102(2017), 1057-1065

DOI: https://doi.org/10.2138/am-2017-5832

A XAFS spectroscopic study of the chemical state of "invisible" Au in synthetic minerals in the Fe-As-S system

Alexander L. Trigub[2,1,8], Boris R. Tagirov[1]*, Kristina O. Kvashnina[3,9], Dmitriy A. Chareev[4,1,7], Maximilian S. Nickolsky[1], Andrey A. Shiryaev[5,1], Nina N. Baranova[6], Elena V. Kovalchuk[1] and Andrey V. Mokhov[1]

[1] Institute of Geology of Ore Deposits (IGEM RAS), 35, Staromonetnyi per., 119017 Moscow, Russia

[2] National Research Centre 'Kurchatov Institute', 1 Akademika Kurchatova Sq., 123182 Moscow, Russisa

[3] ID26 beamline, ESRF, 38043 Grenoble, France

[4] Institute of Experimental Mineralogy (IEM RAS), 142432 Chernogolovka, Moscow Region, Russia

[5] Institute of Physical Chemistry and Electrochemistry (IPCE RAS), 31 korp. 4, Leninsky Prospect, 119071 Moscow, Russia

[7] Institute of Physics and Technology, Ural Federal University, Mira st., 19, 620002 Ekaterinburg, Russia

[8] Physico-Technical Institute of UB RAS, Kirova st. 132, 426000 Izhevsk, Russia

[9] Helmholtz-Zentrum Dresden-Rossendorf (HZDR), Institute of Resource Ecology, P.O. Box 510119, 01314, Dresden, Germany

* corresponding author, E-mail: boris1t@yandex.ru

Keywords: invisible gold, pyrite, arsenopyrite, löllingite, synthetic minerals, X-ray absorption spectroscopy, atomic charges

Submitted to American Mineralogist April 2016

Abstract

Minerals of the Fe-As-S system are ubiquitous components of Au ores in many deposits of hydrothermal origin, including world-class volcanogenic massive sulfide, low-temperature epithermal and mesothermal ones. The “invisible” (or refractory) form of Au is present in all types of hydrothermal ores and in many cases predominates. Knowledge of the “invisible” Au chemical state (local atomic environment/structural position, electronic structure and oxidation state) is a fundamental problem crucial for understanding conditions of the ore formation, is necessary for physical-chemical modeling of hydrothermal Au mineralization, and will help to create more efficient technologies of ore concentration and Au extraction. We report investigation of the “invisible” Au chemical state in synthetic analogues of natural minerals: pyrite (FeS_2), arsenopyrite (FeAsS), and löllingite ($FeAs_2$). The compounds were synthesized using hydrothermal (pyrite) and salt flux techniques (all the minerals) and studied using X-ray absorption fine structure spectroscopy (XAFS) in high energy resolution fluorescence detection (HERFD) mode in combination with first-principles quantum chemical calculations. The concentration of the “invisible” Au in the synthesized löllingite (800±300 ppm) was much higher compared to arsenopyrite (23±14 ppm), whereas the lowest Au content with zonal Au concentration profiles was observed in crystals of salt flux pyrite. The concentration of Au in the hydrothermal pyrite (40-90 ppm) is independent on sulfur fugacity and probably reflects the maximum Au solubility at the experimental *P*/*T* parameters (450 °C, 1 kbar). It is shown that Au replaces Fe in structure of löllingite, arsenopyrite, and hydrothermal pyrite. The nearest-neighbors Au-ligand distance increases by 0.14 Å (pyrite), 0.16 Å (löllingite), and 0.23 (As), 0.13 (S) Å for arsenopyrite relative to Fe-ligand distance in pure compounds. Distortion of the local atomic structure around the Au is negatively correlated with the distance and disappears at r > ~4 Å. The chemically bound Au is stable only in hydrothermal pyrite, whereas the pyrite synthesized in the absence of hydrothermal fluid contains only Au°. Heating (metamorphism) of hydrothermal pyrite results in decomposition of the chemically bound Au with formation of Au°

nuggets which coarsen with temperature. Depending on chemical composition of the host mineral Au can play a role either of cation or anion: the Bader atomic partial charges of Au decrease in the order of pyrite (+0.4 e) > arsenopyrite (0) > löllingite (-0.4 e). Our results suggest that other noble metals (platinum group elements, Ag) can form the chemically bound refractory admixture in base metal sulfides/chalcogenides. The chemical state, as well as the concentration, of this form of noble metals can differ depending on the composition of the host mineral and the ore history.

Introduction

Ores of volcanogenic massive sulfide (VMS) deposits and many types of hydrothermal gold deposits are important source of Au, many of them belong to the world-class gold mines (>100 t Au, Genkin et al., 1998; Mercier–Langevin et al., 2011). In these ores Au can exist as: i) discrete minerals – compounds with chalcogens (S, Se, Te), semimetals (As, Sb, Bi), or intermetallic compounds with Cu, Ag, Hg etc., and ii) the "invisible" (or refractory) state – e.g., nanoscale particles and isomorphous solid solution. The free Au can be effectively extracted from the ore using, for example, cyanide leaching, whereas the "invisible" state makes problematic the Au extraction into commercial concentrates and results in loss of economically important quantities of Au. In many deposits the proportion of "invisible" gold can be very high. For example, at Uchaly deposit in South Urals, Russia it reaches 85%, and the total loss of Au from VMS deposits in South Urals region is 10-15 t Au per year (Vikentyev, 2015). In ores of VMS deposits pyrite (FeS_2) is known to host the maximum concentrations of "invisible" Au, whereas arsenopyrite (FeAsS) is an important Au-bearing mineral in epithermal and low temperature mesothermal deposits (Genkin et al., 1998; Widler and Seward, 2002; Wagner et al., 2007). Understanding the chemical state of Au in sulfide ores will help to constrain conditions at which the ore was formed, is necessary for physical-chemical modeling of hydrothermal Au mineralization, and will have important implications for mineral processing industry. In addition, synthesis of minerals at contrasting *T*/*P* conditions using different experimental techniques followed by determination of the chemical state of Au will help to reveal the effect of the ore formation history, including metamorphic events, on the speciation of Au in sulfides.

In view of fairly low concentration, the chemical state of Au in sulfide ore, including local atomic environment, position in the host mineral structure in case of isomorphous solid solution, and its valence state can be unambiguously revealed only using spectroscopic methods. Published spectroscopic studies were performed using X-ray photoelectron (XPS, see Widler and Seward, 2002 and references cited; Laptev and Rozov, 2006), Mössbauer (Cardile et al., 1993;

Genkin et al., 1998; Kozerenko et al., 2001), and X-ray absorption near edge structure (XANES) spectroscopy (Simon et al., 1999; Cabri et al., 2000). The present study aims at investigation of the chemical state of the "invisible" Au in pyrite, arsenopytite, and löllingite ($FeAs_2$) using X-ray absorption spectroscopy (XAS). We synthesized the Au-bearing chalcogenides, characterized the concentration and distribution of Au in these samples and addressed the Au local environment using XAS. These data were combined with first-principles quantum chemical calculations and Bader charge analysis in order to reveal the local atomic environment and oxidation state of Au in these minerals.

Experimental

Synthesis of minerals and analytical methods

Synthesis experiments were performed using hydrothermal (450 °C, 1 kbar) and salt flux technique (520 – 650 °C). In all the experiments the system was saturated with respect to $Au_{(cr)}$ by placing a piece of Au foil or wire in the autoclave or silica glass ampoule together with initial reagents. The hydrothermal method was used only for synthesis of pyrite, whereas the salt flux experiments were preformed to obtain crystals of Au-bearing pyrite, löllingite, and arsenopyrite. Chemical composition of the synthesized phases was determined using electron microprobe (EPMA), laser ablation inductively coupled mass spectrometry (LA-ICP-MS), and, for hydrothermal pyrite, wet chemistry. Details of the synthesis procedure and analytical methods are given in Supplementary Methods.

XAFS spectroscopic measurements

XAFS spectra were collected at the high-brilliance X-ray absorption and X-ray emission spectroscopy undulator beamline ID26 (Gauthier et al., 1999) of the European Synchrotron Radiation Facility (ESRF) in Grenoble. The incident energy was selected using the <111> reflection from a double Si crystal monochromator. Rejection of higher harmonics was achieved

by three Cr/Pd mirrors positioned at an angle of 2.5 mrad relative to the incident beam. The incident X-ray beam had a flux of approximately $2 \cdot 10^{13}$ photons s^{-1} on the sample position. XANES spectra were simultaneously measured in total fluorescence yield (TFY) mode using a photodiode and in high energy resolution fluorescence detection (HERFD) mode using an X-ray emission spectrometer (Glatzel and Bergmann, 2005; Kvashnina and Scheinost, 2016). The sample, analyzer crystal and photon detector (silicon drift diode) were arranged in a vertical Rowland geometry. The Au XANES/EXAFS HERFD spectra at the L_3 edge were obtained by recording the intensity of the Au $L\alpha_1$ emission line (9713 eV) as a function of the incident energy. The emission energy was selected using the <660> reflection of spherically bent four Ge crystal analyzers (1m curvature radius) aligned at 80° Bragg angle. A combined (incident convoluted with emitted) energy resolution of 1.2 eV was determined by measuring the elastic peak. The intensity was normalized to the incident flux.

For heating experiments a powder of hydrothermal pyrite was placed into the silica glass capillary (Polymicro Technologies™, 350 μm OD, 200 μm ID, length 20 mm) together with small amount of sulfur which prevented oxidation of the sample and controlled sulfur fugacity $f(S_2)$ during the experiment. The capillary was evacuated and hermetically sealed. This simple experimental technique was developed for Raman spectroscopic studies of solids and liquids (Chou et al., 2008, 2012; Ding, 2010), and in the present study we adopted it for the synchrotron experiment. The *in situ* XAS measurements were performed with capillaries placed into Microtomographic furnace available at ESRF. The temperature readings of thermocouple were calibrated using K-type thermocouple placed in contact with the capillary to the accuracy of ±5 °C.

Density Functional Theory (DFT) calculations

QUANTUM ESPRESSO software package (Giannozzi et al., 2009) was used for quantum chemical DFT calculations. We employ projector-augmented wave (PAW) all-electron

description of the electron-ion-core interactions (Blöhl, 1994; Kresse, 1999) and the Perdew-Burke-Ernzerhof (PBE) exchange-correlation functional. For the electronic structure calculations self-consistent field (SCF) method was applied with 100 Ry kinetic energy cutoff for the plane waves, 1500 Ry charge density cutoff, and SCF tolerance better than 10^{-9}. Optimization of the crystal structure and supercell parameters were performed using the BFGS algorithm for atomic coordinates with convergence threshold 10^{-3} Ry/au for forces and 10^{-4} Ry for energy. The relaxation of the atomic positions and cell parameters were performed in a supercell which contained 2×2×2 unit cells for pyrite and arsenopyrite, and 2×2×3 unit cells for löllingite. Topological atomic charges were determined by means of the quantum theory of atoms in molecules (QTAIM). The local atomic charges were calculated by integrating the charge density within Bader volumes around atoms (Otero-de-la-Roza et al., 2009; Otero-de-la-Roza et al., 2014).

EXAFS spectra analysis

Analysis of the EXAFS spectra allowed determination of Au local atomic environment. The EXAFS data ($\chi_{exp}(k)$) were analyzed using IFEFFIT data analysis package (Ravel and Newville, 2005). Following standard procedures for pre-edge subtraction and spline background removal, the structural parameters such as interatomic distances (R_i), coordination numbers (N_i), and Debye–Waller factors (σ^2) were found by the non-linear fit of theoretical spectra to the experimental with the equation

$$\chi(k) = S_0^2 \sum_{i=1}^{n} \frac{N_i F_i(k)}{R_i^2 k} e^{\frac{-2R_i}{\lambda(k)}} e^{-2\sigma_i^2 k^2} \sin\left(2kR_i + \varphi_i(k)\right) \qquad (1)$$

The theoretical spectra were simulated using the photoelectron mean free path $\lambda(k)$, amplitude $F_i(k)$, and phase shift $\varphi_i(k)$ calculated *ab initio* using program FEFF6 (Zabinski, 1995). This calculation method yields the statistical uncertainty of 0.01–0.02 Å for the refined R_i in the first coordination shell.

XANES spectra simulation

Theoretical calculations of the Au L_3 edge spectra were performed using two methods: finite difference method (FDM) and full multiple scattering (FMS). The FDM is realized in FDMNES code (Joly, 2001; Guda, 2015). Relativistic self-consistent field FDMNES calculations were carried out with the exchange-correlation part of potential in a local density approximation (Hedin and Lundqvist, 1971). The final electronic states were calculated in a full core hole screening. Atomic clusters inside the spheres with radii of 8 Å and 7 Å were chosen for self-consistent calculations and for FDM XANES calculations, respectively. Despite the fact that this calculation procedure is computationally expensive, it represents the best choice for systems with non-spherical charge distribution. To account for many body effects and core hole lifetime broadening, the arctangent convolution was applied (Bunău and Joly, 2009).

The FMS spectra modeling was performed using FEFF9.6 revision 4 code (Rehr, 2010), which is based on the self-consistent muffin-tin potentials. The Dirac-Hara exchange-correlation potentials were used. The parameter for the imaginary potential was set to -2 to account for the reduced broadening of HERFD XANES spectra. Self-consistent calculations were refined with a radius of 6 Å around the central Au atom, whereas for the FMS calculations we have chosen a radius of 7 Å. The RPA core hole approximation was applied to simulate the central excited atom.

Results

Concentration and distribution of Au in synthesized minerals

Pyrite FeS_2. Concentrations of Au in hydrothermal pyrites and coexisting aqueous fluid (450 °C, 1 kbar) are presented in Supplementary Table S1 and shown in Fig. 1. The SEM image at the top of Fig. 1 shows that the hydrothermal pyrite consists of fine-grained aggregates with particle size < 10 μm. The powder lacks inclusions of metallic Au and, therefore, the total Au determined by the dissolution of pyrite samples corresponds to concentration of the "invisible" Au. We note

here that the synthesis of pyrite free of inclusions of metallic Au was possible only in acidic solutions with low concentration of Au dissolved in aqueous fluid. Our attempts to increase the concentration of the "invisible" Au in pyrite by performing the synthesis in weakly alkaline solutions with high aqueous Au concentrations (up to 0.1 mol·kg H_2O^{-1}, or $2 \cdot 10^5$ ppm) yield mixture of pyrite and Au metal. Example of synthesized material is shown in Fig. S1, the concentration of Au determined in pure FeS_2 grains obtained in these experiments was close to EPMA detection limit of 100 ppm.

In the hydrothermal experiments the sulfur fugacity was buffered due to the elemental sulfur dissolution and hydrolysis reactions (see Supplementary Methods). The concentration of Au in aqueous fluid increases with $f(S_2)$. The slope S of the linear fit of the experimental Au solubility data plotted as log m(Au) vs. log $f(S_{2(g)})$ is equal to 0.67. This means that $AuHS°_{(aq)}$ dominates aqueous Au speciation. For this complex the slope of the solubility curve S= 0.5 as given by,

$$Au_{(cr)} + 0.5\ S_{2(g)} + 0.5\ H_{2(g)} = AuHS°_{(aq)} \quad , \quad (2)$$

as $f(H_{2(g)})$ is the same for all the experimental points (except the S + H_2SO_4 experiment). Increase of the slope observed in our experiments can be caused by the presence of $Au(HS)_2^-$ and/or by the uncertainty in the calculated $f(S_{2(g)})$ values.

Effect of sulfur on the concentration (solubility) of Au in solid sulfide determines the stoichiometry of the solubility reaction (the number of S_2 molecules interacting with Au to form the Au-bearing pyrite),

$$Au_{(cr)} + n/2\ S_{2(g)} = AuS_{n(sulfide)} \quad (3)$$

and, therefore, the Au/S concentration ratio and the formal oxidation state of Au in sulfide. In contrast to Au solubility in the aqueous fluid, the concentration of Au in the hydrothermal pyrite is weakly sensitive to $f(S_2)$ and oxidation potential and always falls within 40 – 90 ppm concentration range (Table S1). We consider this value as the upper Au concentration limit for *T*/*P* conditions of the synthesis experiments. Formally, the slope *S* ~0 may indicate that Au does not interact with dissolved sulfur and, therefore the oxidation state of Au in the sulfide remains unchanged with respect to metal. However, the true (not formal) structural position and the valence state of Au distributed in the sulfide mineral matrix can only be determined by means of spectroscopic experiments described in the following section.

Grains of high-temperature pyrite synthesized at 620 °C using the salt flux method reveal zonal Au concentration profiles with C(Au) extending from detection limit to several hundred ppm (Table S2). The smooth character of Au time-resolved laser-ablation-ICP-MS spectra shown in Fig. S2, suggests that microscopic and submicroscopic inclusions of Au are absent, but the LA-ICP-MS data alone do not enable to unambiguously determine the chemical state of Au. It is interesting to note that in addition to Au this sample of pyrite contains ppm level of Pt, trace amount of which was accidentally introduced into the charge.

Arsenopyrite FeAsS and löllingite $FeAs_2$. Examples of synthesized crystals of arsenopyrite and löllingite are shown in Supplementary Figs. S3 and S4, respectively. Time-resolved LA-ICP-MS profiles for Au through grains of these minerals are presented in Figs. S5 and S6. Two types of LA-ICP-MS spectra were observed in arsenopyrite. The first contains Au-rich and Au-poor zones with Au concentration of several hundreds and up to 30 ppm, respectively (top of Fig. S5). The second type of the profiles corresponds to homogeneously distributed Au with C(Au) ~10 ÷ 30 ppm (Fig. S4, bottom). In the löllingite Au is distributed homogeneously and C(Au) = 800 ± 300 ppm (Fig. S6). Note that the concentration of the “invisible” Au in the löllingite is much higher compared to the arsenopyrite, whereas the lowest Au content was determined in pyrite crystals synthesized by the salt flux technique.

XANES spectroscopy

Ambient temperature experiment. The HERFD-XANES spectroscopic technique made possible acquisition of the Au L_3 spectra not only for pyrite but also for arsenopyrite and löllingite where the signal from trace amount of the "invisible" Au is masked by As K edge in the TFY mode (Fig. 2). Another advantage of high-energy resolution technique is that weak features of the Au(I) spectra are considerably enhanced in comparison with TFY spectroscopy thus facilitating interpretation and modeling. Figure 3a shows Au L_3 HERFD-XANES spectra of the Au-bearing pyrite (hydrothermal), arsenopyrite, and löllingite together with spectra for model substances. All these minerals contain Au in the chemically bound state which is different from both $Au_{(cr)}$ and Au_2S. Positions of the edge jump (e.j.) and the first intense feature (white line, WL) are listed in Table 1. We observe significant positive energy shift of the e.j. position in the order of pyrite < arsenopyrite < löllingite. Positive e.j. shift usually indicates increase of the positive charge of the excited atom. However, as it will be shown below, this is not the case for the Fe-As-S system.

The Au L_3 edge absorption is related to $2p$-$5d$ dipole-allowed transitions: $2p_{3/2} \rightarrow 5d_{5/2}$ /$5d_{3/2}$. Therefore, the WL intensity reflects the number of empty states in the $5d_{5/2}$ and $5d_{3/2}$ orbitals above the Fermi level. The WL intensity for arsenopyrite and löllingite is much greater than for pyrite (Fig. 3a), indicating higher number of holes in the $5d$ electronic shell of As-bearing minerals. Another important difference of the Au L_3 edge HERFD-XANES spectra of these minerals is negative correlation between intensity of the second feature at ~11929 eV with As content. This feature is clearly visible in the spectra of the Au-bearing pyrite, the arsenopyrite spectra contains only traces of the feature, and it is absent in the spectra of löllingite.

Figure 3b compares spectra of arsenopyrite and löllingite to the spectra of model systems – synthetic $AuSb_2$ and Au_2Bi. This figure, together with Table 1, indicates significant positive shift of the e.j. position in the order of $AuSb_2$ < Au_2Bi < Au in arsenopyrite < Au in löllingite.

This order corresponds to decrease of the number of the chemical element in the 15^{th} group of the periodic system and implies that Au is chemically bound to As in arsenopyrite and löllingite matrices.

Pyrite heating experiment. This experiment was aimed at modeling the behavior of the "invisible" Au during hydrothermal ores metamorphism. Results of the experiment are presented in Fig. 4. The spectra collected at ambient temperature show that the chemical states of Au in hydrothermal and salt flux pyrites differ. The chemically bound "invisible" Au exists only in the hydrothermal pyrite. Large well crystallized grains of pyrite formed in the eutectic anhydrous chloride mixture contain mostly metallic Au°. Heating of the hydrothermal pyrite to 460 °C results in decomposition of the chemically bound Au with precipitation of Au°. Note that this process takes place even in the presence of $S_{(l)}$ which should promote the formation of the Au-bearing solid solution (Eq. 3). Further heating to 630 °C results in dramatic drop of the XAFS signal; the spectrum at this temperature corresponds to traces of Au in the chemically bound state. This can be explained by coalescence of Au nanoparticles into few larger particles. Due to relatively small beam spot the amount of gold in the beam drops dramatically. These data are consistent with analyses of natural Au-bearing arsenopyrite ores reported in Wagner et al. (2007) where it was shown that metamorphism results in decrease of Au concentration in arsenopyrite. The irreversible process of Au nanoparticles coarsening during heating of the arsenian pyrite was observed using in situ transmission electron microscopy (Reich et al., 2006). Our results demonstrate that heating (metamorphism) of Au-bearing pyrite ore results in decomposition of the chemically bound "invisible" Au incorporated into hydrothermal pyrite matrix during ore-forming process.

EXAFS analysis

EXAFS spectra for the pyrite and löllingite are shown in Fig. 5. Contamination with metallic Au° hampered record of good quality EXAFS spectra for the arsenopyrite, therefore in

the present study we use only XANES spectra to model the chemical state of Au in this mineral. EXAFS spectra of pyrite and löllingite shown in Fig. 5 are different: the maxima of the EXAFS function are clearly shifted to higher *k* values for the löllingite. The main peak in the Fourier transforms (FTs) of the löllingite EXAFS function (Fig. 5, bottom) is at higher values of *R*, reflecting larger Au-L distance in the first coordination shell. Results of the least-square fit of the FTs are shown by thick red lines in Fig. 5 and calculated model parameters are listed in Table 2. For both minerals the best fit of the experimental spectra is achieved when Au replaces Fe in the host mineral structure. In accord with structures of these minerals (see Supplementary Structures) the metal atom is octahedrally coordinated with ligands in the first coordination shell. For pyrite the first neighbors around Au are 6 S atoms at 2.40 Å, and for löllingite – 6 As atoms at 2.52 Å. Due to large Au ionic radius the Au-L distances increase by 0.14 and 0.16 Å compared to the crystal structures of pure pyrite and löllingite, respectively. The distortion of the local environment around Au in pyrite decreases to 0.06 – 0.08 Å for S atoms in the second coordination shell, whereas the Au-Fe distance for the nearest Fe atoms at ~3.8 Å remains unchanged within uncertainty of EXAFS fit (0.04 – 0.05 Å for distant coordination shells). Similar picture is observed for löllingite: the distortion of the crystalline structure decreases for distant coordination shells and disappears at $r > 4.2$ Å.

DFT calculations

The interatomic distances optimized by DFT method for pyrite and löllingite are listed in Table 2. For löllingite good agreement is observed between the simulated structure and results of the EXAFS spectra fit for the first and second neighbors (within 0.02 Å for the first coordination shell at 2.5 Å and 0.03 Å for the second shell at 3 Å). Similar results were obtained in our recent study of Au-bearing covellite CuS where the EXAFS model was correctly reproduced by DFT simulation at distances up to 4 Å (the agreement between DFT calculations and EXAFS fitting was within 0.01 – 0.04 Å depending on the distance, Tagirov et al., 2016). Based on these results we can suggest that our method of DFT calculation can reproduce atomic coordinates of Au-

bearing chalcogenides within 0.02 and 0.04 Å at least for the first two coordination shells located at distances up to 3 Å.

For pyrite the agreement between the DFT simulation and EXAFS fit is poor: the difference is 0.055 Å for the first neighbors around Au atom. This fact can be explained by thermodynamic instability of Au-bearing pyrite whose atomic environment can not be accurately reproduced by the equilibrium structure relaxation methods. This finding is consistent with results of pyrite heating experiment where the chemically bound Au decomposes at high temperature and leave the FeS_2 matrix. Note that as a general rule increase of temperature stabilizes solid solutions, whereas the opposite was observed in the case of Au- bearing pyrite.

Table 3 reports results of DFT simulation of the local atomic environment for Au-bearing arsenopyrite. The distances Au-S and Au-As in the first coordination shell increased by 0.13 and 0.23 Å, respectively. The Au-Fe distance for the nearest two Fe atoms increased by 0.25 Å with respect to the pure arsenopyrite. This model will be checked via Au L_3 edge HERFD-XANES spectra modeling.

XANES spectra simulation

Results of the Au L_3 edge HERFD-XANES spectra modeling are shown in Fig. 6a-c. For Au in pyrite spectra (Fig. 6a) the FDMNES calculations overestimate the WL intensity and shift the second feature by ~-2 eV relatively to the experimental spectrum. This disagreement probably stems from the metastable nature of the “invisible” Au in pyrite which leads to shortcomings in the FDM SCF-based spectra modeling. The spectrum calculated using FEFF9 computer code is given for comparison. The agreement between experimental and simulated spectra is good with exception of the third diffuse feature with centroid at ~11945 eV which is absent in the calculated spectrum.

The FDMNES calculation for löllingite (Fig. 6b) is in good agreement with the experimental spectrum. The only difference is overestimated width of the WL. The second

feature present in the spectra of Au-bearing pyrite at 11927 eV is almost invisible in the calculated and experimental löllingite spectra. Intensity and positions of the spectral features for the Au-bearing arsenopyrite are correctly reproduced by the FDMNES calculation (Fig. 6c) which supports results of the DFT calculation for this mineral.

The valence state of the "invisible" Au

Results of Bader analysis of the electron density performed using QTAIM for the pure and Au-bearing minerals are presented in Table 3. For the pure minerals partial atomic charges of S atoms are more negative than the charge of As (-0.7 e for disulfide group in pyrite vs. -0.08 e for As in löllingite). In arsenopyrite the topological charge of As is positive and equal to +0.18 e, whereas S is negatively charged (-0.6 e). These atomic partial charges reflect distribution of delocalized electrons and are in line with Pauling electronegativity: $\chi(S) = 2.58 >> \chi(As) = 2.18$ (Hui et al., 2000). For the Au-bearing minerals negative atomic charges of Au increase systematically in order pyrite > arsenopyrite > löllingite. The Au atom is positively charged in pyrite, about neutral in arsenopyrite, and plays a role of anion in löllingite. Note that the charge of Au in löllingite is much more negative than As. This is explained by the fact that Au is the most electronegative metal ($\chi(Au) = 2.54$) whose electron affinity is higher than that of semi-metals.

Discussion and implications

Results of our study demonstrate that Au substitutes for Fe in crystal structures of pyrite, arsenopyrite, and löllingite. However, chemical nature of the "invisible" Au in these minerals differs. In pyrite the chemically bound Au is formed only in presence of the hydrothermal solution. These results are consistent with study of Au adsorption by pyrite performed by Widler and Seward (2002). They found that Au can be effectively scavenged by natural and synthetic pyrites at acidic pH where $AuHS°_{(aq)}$ is the dominant Au complex in aqueous solution. Similar

Au adsorption isotherms were observed for As_2S_3 and Sb_2S_3 by Renders and Seward (1989). In view of these results our observation that Au concentration in pyrite is independent on $f(S_2)$ (and, therefore, on concentration of $AuHS°_{(aq)}$) can be explained by attainment of the maximum pyrite sorption capacity with respect to Au. At the same time, pyrite grains synthesized using dry salt melt as a transport medium contain only Au°. Similarly, heating of the hydrothermal pyrite in dry system results in decomposition of the chemically bound Au.

The XPS measurements by Widler and Seward (2002) on Au-bearing pyrites showed that the chemical state of Au in pyrite is different from Au°. The Au $4f_{7/2}$ electron binding energy (*BE*) is 84.8 eV for Au in pyrite whereas for metallic Au *BE* = 84.0 eV. Close value of *BE* = 85.1 eV was measured for Au-bearing pyrite synthesized at 200 °C (Laptev and Rozov, 2006). This value is higher than Au $4f_{7/2}$ *BE* in Au_2S where Au is linearly coordinated with two S atoms (BE_{Au/Au_2S} ~84 eV, Tagirov et al., 2014), implying that local environments of Au in pyrite and Au_2S differ. However, the core level XPS technique is less sensitive to local atomic environment geometry and chemical bonding compared to XAFS spectroscopy, which is able to unambiguously determine the chemical state of Au.

The concentration of the chemically bound "invisible" Au in pyrite determined in the present study for 450 °C hydrothermal experiment (tens of ppm) is somewhat below the maximum concentration of $\sim10^2$ ppm measured in pyrite synthesized by Laptev and Rozov (2006) at 200 °C and $\sim1\text{-}3\cdot10^2$ ppm in the ambient temperature sorption experiments of Widler and Seward (2002). Neglecting the differences in the surface area or grain size, which usually falls within $1\div n\cdot10$ μm for fine-grained pyrite, we can estimate the maximum possible concentration of the chemically bound Au in hydrothermal pyrite formed in 25-450 °C temperature interval as 30 ppm (< C(Au) < 300 ppm. Temperature increase results in decrease of the adsorbed Au concentration and the maximum concentration of the chemically bound "invisible" Au in pyrite can be roughly estimated as: 100-300 ppm at 25 °C, 130 ppm at 100 °C, 100 ppm at 200 °C, 70 ppm at 300 °C, 60 ppm at 400 °C, and 50 ppm at 500 °C, showing,

therefore, retrograde behavior. One should expect that excess of Au will be present in the metallic state.

In contrast to pyrite, Au can form isomorphous solid solution with arsenopyrite and löllingite even at high temperatures (> 500°C) in the absence of aqueous fluid. This suggests thermodynamic stability of this form of the chemically bound Au in these minerals. The maximum concentration of the chemically bound "invisible" Au was determined as tens ppm for arsenopyrite and hundreds ppm for löllingite. These data are consistent with analyses of natural ores which show that As stabilizes Au-bearing sulfides and results in increase of the gold concentration (c.f. Reich et al., 2005).

Comparison of the Au L_3 HERFD-XANES spectra shows that edge energy (e.j.) increases when As replaces S in the order of pyrite < arsenopyrite < löllingite (Table 1, Fig. 3a). Usually this means that the atomic charge increases in the same order becoming more positive for higher e.j. values (higher energy is necessary to excite the core level electron). However, data of Table 4 shows that the opposite is true: Au is positively charged in pyrite and negatively - in löllingite (Table 4). This e.j. behavior can not be explained by the effect of the atomic charge alone and needs further examination.

The WL position and intensity indicates that the number of Au 5*d* unoccupied electronic states increases in the As-bearing phases relatively to pyrite despite the fact that Au is more electronegative than As. This unusual picture can be explained by the charge compensation model which was developed to describe the charge flow in Au alloys (Watson et al., 1971). In this model Au loses *d*-charge upon alloying, but it is overcompensated by a gain of a conduction (mainly *s*-*p*) charge from the second alloy component. As a result, Au gains the overall negative charge (see Kuhn and Sham, 1994; Bzowski et al., 1995, and literature cited). The fact that Au can change its valence state depending on the host mineral composition demonstrates that there is no need in coupled charge compensation substitution for the formation of isomorphous solid solutions in crystals with high degree of the chemical bond covalency.

Along with Au the other noble metals (platinum group elements, Ag) often exist in the form of the “invisible” admixture in sulfide ore. Considering their chemical state in sulfide minerals from the point of view of the present study we can suggest that these metals also can form the chemically bound refractory admixture. The chemical state as well as the concentration of this form of noble metals can differ with respect to the local atomic environment/structural position and valence state depending on the composition of host sulfide and the ore history (e.g., hydrothermal, magmatic, or metamorphic). Further spectroscopic studies, including in situ X-ray absorption/emission spectroscopy experiments performed at high *T*/*P* parameters will help to reveal the chemical state of noble metals and discover regularities of the ore-forming processes.

Acknowledgments: Authors acknowledge the ESRF for the beamtime allocation under proposals ES-184 and ES-360. The help and support of Sara Lafuerza and Pieter Glatzel during the beam time are greatly appreciated. B.R.T. and K.O.K. thank Hugo Vittoux for outstanding technical support during the in-situ experiment with micro-furnace at ID26 beamline. We are grateful to Sara-J. Barnes for organizing the LA-ICP-MS measurements at the University of Chicoutimi, V. Abramova and E. Minervina for chemical analyses of synthesized minerals using LA-ICP-MS methods. . The results of this work were obtained using computational resources of MCC NRC “Kurchatov Institute” (http://computing.kiae.ru/). This study was supported by Russian Scientific Foundation grant No. 14-17-00693. D.Ch was involved in Act 211 Government of the Russian Federation, agreement № 02.A03.21.0006 (synthesis of sulfides via salt flux technique).

References cited

Bayliss, P. (1977) Crystal structure refinement of weakly anisotropic pyrite cubic model. American Mineralogist, 62, 1168-11782.

Bindi, L., Moelo, Y., Leone, P., and Suchaud, M. (2012) Stoichiometric arseonpyrite, FeAsS, from La Roche-Balue Quarry, Loire-Atlantique, France: Crystal structure and Mossbauer study. The Canadian Mineralogist, 50, 471-479.

Blöhl, P.E. (1992) Projector augmented-wave method. Physical Review B, 50, 17953–17979.

Bortnikov, N.S., Cabri, L.J., Vikentiev, I.V., Tagirov, B.R., Mc Mahon, G., Bogdanov, Yu.A., and Stavrova, O.O. (2003) Invisible Gold in Sulfides from Seafloor Massive Sulfide Edifices. Geology of Ore Deposits, 45, No. 3, 201-212.

Bzowski, A., Yiu, Y.M., and Sham, T.K. (1995) Charge redistribution in Au-metalloid intermetallics: A Au $L_{2,3}$ –edge x-ray absorption study. . Physical Review B, 51, 9515-9520.

Cabri, L.J., Newville, M., Gordon, R.A., Daryl Crozier, E., Sutton, S.R., Mcmahon, G., and Jiang, D.T. (2000) Chemical speciation of gold in arsenopyrite. The Canadian Mineralogist, 38, 1265-1281.

Cardile, C.M., Cashion, J.D., McGrath, A.C., Renders, P., and Seward, T.M. (1993) ^{197}Au Mössbauer study of Au_2S and gold adsorbed onto As_2S_3 and Sb_2S_3 substrates. Geochim. Cosmochim. Acta 57, 2481-2486.

Chou, I-M. (2012) Optical cells with fused silica windows for the study of geological fluids. In J. Dubessy, M.-C. Gaumont and F. Rull Eds., Applications of Raman Spectroscopy to Earth Sciences and Cultural Heritage, 12, p. 227-248. EMU Notes in Mineralogy, London.

Chou, I-M., Song, Y., and Burruss, R. C. (2008) A new method for synthesizing fluid inclusions in fused silica capillaries containing organic and inorganic material. Geochim. Cosmochim. Acta, 72, 5217-5231.

Ding, J. (2010) The pH determination of palaeofluids: experimental and thermodynamic approach, 173 p. PhD thesis, Université Henri Poincaré, Nancy.

Gauthier, C., Sole, V.A., Signorato, R., Goulon, J., and Moguiline, E. (1999) The ESRF beamline ID26: X-ray absorption on ultra dilute sample. Journal of Synchrotron Radiation, 6, 164-166.

Genkin, A.D., Bortnikov, N.S., Cabri, L.J., Wagner, F.E., Stanley, C.J., Safonov, O.G., McMahon, G., Friedl, J., Kerzin, A.L., and Gamyanin, G.N. (1998) A multidisciplinary study of invisible gold in arsenopyrite from four mesothermal gold deposits in Siberia, Russian federation. Economic Geology, 93, 463-487.

Giannozzi, P., Baroni, S., Bonini, N., Calandra, M., Car, R., Cavazzoni, C., Ceresoli, D., Chiarotti, G.L., Cococcioni, M., Dabo, I. and others (2009) QUANTUM ESPRESSO: a modular and open-source software project for quantum simulations of materials. Journal of Physics: Condensed Matter, 21, 395502.

Glatzel, P., and Bergman, U. (2005) High resolution 1s core hole X-ray spectroscopy in 3d transition metal complexes - electronic and structural information. Coordination Chemistry Reviews, 249, 65-95.

Huheey, J.E., Keiter, E.A., and Keiter, R.L. (2000) Inorganic chemistry. Principles of structure and reactivity. 4th edition, Pearson Education.

Joly, Y. (2001). X-ray absorption near-edge structure calculations beyond the muffin-tin approximation. Physical Review B, 63, 125120-125129.

Kozerenko, S.V., Wagner, F.E., Friedl, J., and Fadeev, V.V. (2001) Gold in pyrite formation processes: 3. Mössbauer study of synthetic gold-bearing iron sulfides. Geochemistry International, 39, Suppl. 2, S167-S172.

Kresse, G. (1999). From ultrasoft pseudopotentials to the projector augmented-wave method. Physical Review B, 59, 1758–1775.

Kuhn, M., and Sham, T.K. (1994) Charge redistribution and electronic behavior in a series of Au-Cu alloys. Physical Review B, 49, 1647-1661.

Kvashnina, K.O., and Scheinost, A.C. (2016) A Johann-type X-ray emission spectrometer at the Rossendirf Beamline. Journal of Synchrotron Radiation, accepted.

Laptev, Yu.V., and Rozov, K.B. (2006) Interaction of gold with sulfide surface as a factor of its concentration in hydrothermal ore formation. Doklady Earth Sciences, 411, No. 8, 1229-1232.

Lutz, H.D., Jung, M., and Wäschenbach, G. (1987) Kristallstrukturen des löllingits $FeAs_2$ und des pyrits $RuTe_2$. Zeitschrift für Anorganische und Allgemeine Chemie, 554, 87-91.

Mercier-Langevin, P., Hannington, M.D., Dubé, B., and Bécu, V. (2011) The gold content of volcanogenic massive sulfide deposits. Mineralium Deposita, 46, 509-539.

Morales-García, A., Soares, A. L., Dos Santos, E.C., de Abreu, H.A., and Duarte, H.A. (2014) First-principles calculations and electron density topological analysis of covellite (CuS). Journal of Physical Chemistry A, 118, 5823–5831.

Otero-de-la-Roza, A., Blanco, M.A., Martín Pendás, A., and Luaña, V. (2009) Critic: a new program for the topological analysis of solid-state electron densities. Computer Physics Communications, 180, 157–166.

Otero-de-la-Roza, A., Johnson, E.R., and Luaña, V. (2014) Critic2: A program for real-space analysis of quantum chemical interactions in solids. Computer Physics Communications, 185, 1007–1018.

Ravel, B., and Newville, M. (2005) ATHENA, ARTEMIS, HEPHAESTUS: data analysis for X-ray absorption spectroscopy using IFEFFIT. Journal of Synchrotron Radiation, 12, 537-541.

Reich, M., Kesler, S., Utsunomiya, S., Palenik, C.S., Chryssoulis, S.L., and Ewing, R. C. (2005) Solubility of gold in arsenian pyrite. Geochimica et Cosmochimica Acta, 69, 2781-2796.

Reich, M., Utsunomiya, S., Kesler, S., Wang, L., Ewing, R.C., and Becker, U. (2006) Thermal behavior of metal nanoparticles in geologic materials. Geology, 34, 1033-1036.

Rehr, J.J., Kas, J.J., Vila, F.D., Prange, M.P., and Jorissen, K. (2010). Parameter-free calculations of X-ray spectra with FEFF9. Physical Chemistry Chemical Physics, 12, 5503-5513.

Renders, P.J., and Seward, T.M. (1989) The adsorption of thio gold(I) complexes by amorphous $As_2S_3$and Sb_2S_3 at 25 and 90 °C. Geochimica et Cosmochimica Acta, 53, 255-267.

Simon, G., Huang, H., Penner-Hahn, J.E., Kesler, S., Kao, L.S. (1999) Oxidation state of gold and arsenic in gold-bearing arsenian pyrite. American Mineralogist, 84, 1071-1079.

Tagirov, B.R., Dikov, Yu.P., Buleev, M.I., Koval'chuk, E.V., Chareev, D.A., Kokh, M.A., Borisovskii, S.E., Abramova, V.D., Baranova, N.N., Garas'ko, M.I., Kovalenker, V.A., and Bortnikov, N. S. (2014) "Invisible" gold in covellite (CuS): synthesis and studies by EPMA, LA–ICP–MS, and XPS techniques. Doklady Earth Sciences, 459, Part 1, 1381–1386.

Tagirov, B.R., Trigub, A.L., Kvashnina, K.O., Shiryaev, A.A., Chareev, D.A., Nickolsky, M.S., Abramova, V.D., and Kovalchuk, E.V. (2016) Covellite CuS as a matrix for "invisible gold: X-ray spectroscopic study of the chemical state of Cu and Au in synthetic minerals. Geochimica et Cosmochimica Acta, submitted.

Vikentyev, I.V. (2015) Invisible and microscopic gold in pyrite: methods and new data for massive sulfide ores of the Urals. Geology of Ore Deposits, 57, No. 4, 237-265.

Wagner, T., Klemd, R., Wenzel, T., and Mattson, B. (2007) Gold upgrading in metamorphosed massive sulfide ore deposits: Direct evidence from laser-ablation-inductively-coupled plasma mass spectrometry of invisible gold. Geology, 35, 775-778.

Watson, R.E., Hudis, J., and Perlman, M.L. (1971) Charge flow and *d* compensation in gold alloys. Physical Review B, 4, 4139-4144.

Widler, A.M., and Seward, T.M. (2002) The adsorption of gold (I) hydrosulphide complexes by iron sulphide surfaces. Geochim. Cosmochim. Acta, 66, 383-402.

Zabinsky, S.I., Rehr, J.J., Ankudinov, A., Albers, R.C., and Eller, M.J. (1995) Multiple-scattering calculations of X-ray-absorption spectra. Physical Review B, 52, 2995-3009.

Figure Captions

Figure 1. Results of pyrite hydrothermal synthesis experiment, t = 450 °C, P = 1 kbar. **A -** BSE image of fine-grained aggregate of synthetic pyrite; **b -** concentration of Au in pyrite and coexisting aqueous fluid as a function of sulfur fugacity. Filled circles – sulfur was used to control $f(S_2)$; empty circles correspond to the S + H_2SO_4 system (last row in Table S1), where $f(S_2)$ value has to be corrected.

Figure 2. Difference between the TFY and HERFD spectra for the löllingite sample, C(Au) =800 ppm. In TFY mode the Au features are completely masked by As K edge. The HERFD mode makes possible to record the Au L_3 edge spectra.

Figure 3. The Au L_3 edge HERFD XANES spectra of the Au-bearing pyrite (hydrothermal synthesis, sample 6-16), arsenopyrite, löllingite (salt flux synthesis), and model subnstances. **A** – comparison with $Au_{(cr)}$ and $Au_2S_{(cr)}$; **b** - enlarged energy scale, comparison of arsenopyrite and löllingite with $AuSb_2$ and $AuBi_2$. Note that the spectra of all samples of hydrothermal pyrites shown in Fig. 1 were similar to the specrtra of sample 6-16 shown in this figure.

Figure 4. The Au L_3 edge HERFD XANES spectra of pyrites synthesized using hydrothermal (sample 6-16, C(Au) = 36 ppm) and salt flux techniques (CD-624, C(Au) ~60 ppm, measured concentrations of Au in this sample are listed in Table S2). Heating of hydrothermal pyrite resulted in decrease of signal intensity. At 630 °C the spectra corresponded to the chemically bound Au whose concentration continuously decreased with time during the experiment (see text for explanation). Vertical lines indicate position of 3 main features of $Au_{(cr)}$.

Figure 5. EXAFS spectra of Au-bearung pyrite (*left pannel*, hydrothermal synthesis) and löllingite (*right pannel*, salt flux synthesis). *Top* – background subtracted EXAFS spectra, k^2 weighted; *bottom* – Fourier transforms of the k^2 weighted EXAFS spectra, not corrected for phase shift. Paths are indicated near the FT features. Thin black lines – experiment, thick red lines – fit results.

Figure 6. Resuls of theoretical calculation of Au L_3 edge XANES spectra for Au-bearing pyrite (**a**), löllingite (**b**), and arsenopyrite (**c**). Experimental spectra are shown for comparison (*Pyrite*: sample 6-16, hydrothermal, C(Au) = 36 ppm; *Löllingite*: sample 5333, salt flux synthesis, C(Au)

= 800±300 ppm; *Arsenopyrite*: sample 5140, salt flux synthesis, C(Au) = 23±14 ppm). For pyrite "EXAFS structure" was built by setting the first-neighbour Au-S distances in accordance with the EXAFS model (Table 2), whereas all other distances were adopted from the unrelaxed structure of pure pyrite.

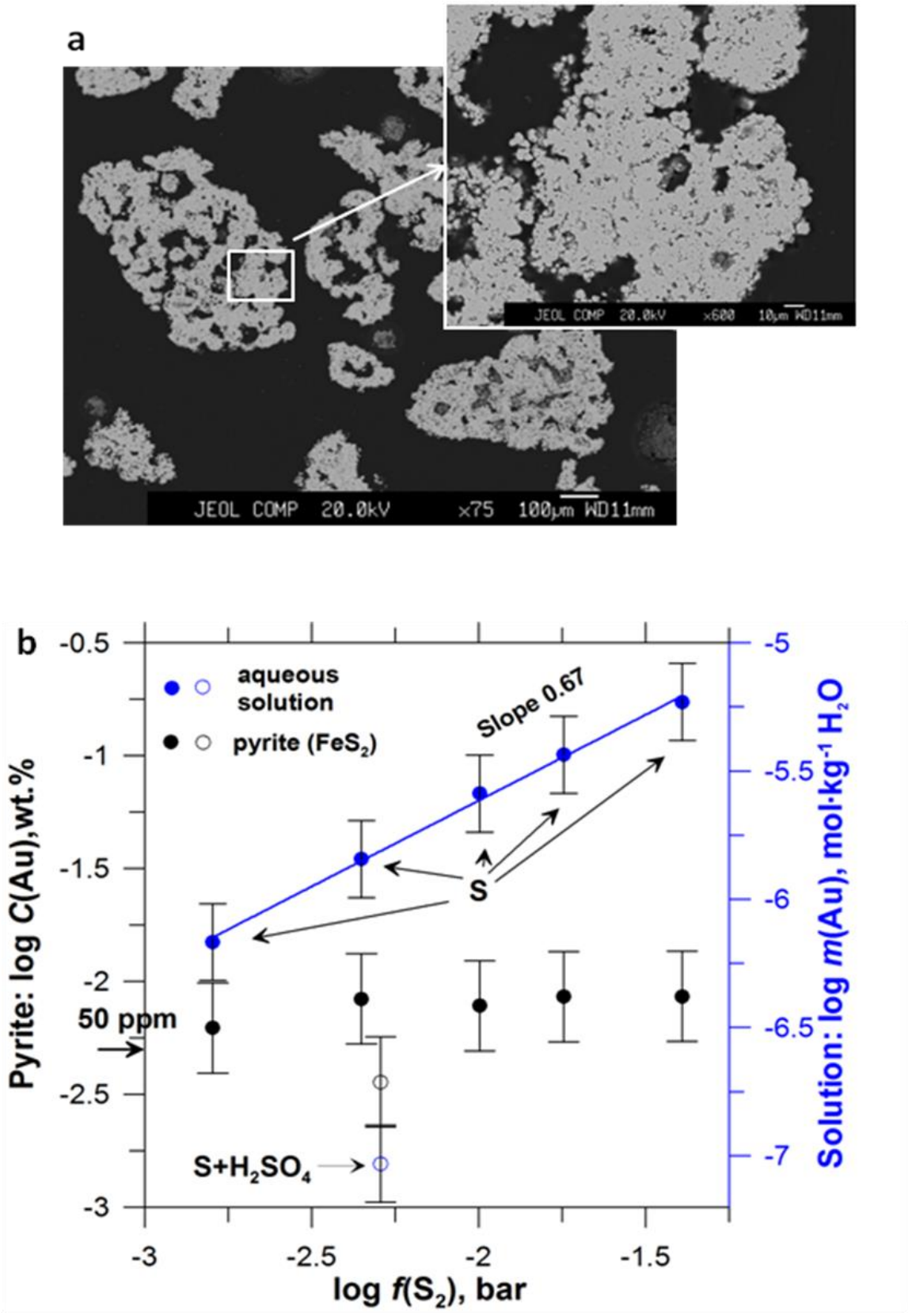
a
JEOL COMP 20.0kV ×75 100μm WD11mm
JEOL COMP 20.0kV ×600 10μm WD11mm
b
aqueous solution
pyrite (FeS2)
Slope 0.67
S
50 ppm
S+H2SO4
Pyrite: log C(Au),wt.%
Solution: log m(Au), mol·kg-1 H2O
log f(S2), bar
-0.5
-1
-1.5
-2
-2.5
-3
-5
-5.5
-6
-6.5
-7
-3
-2.5
-2
-1.5

Fig. 1.

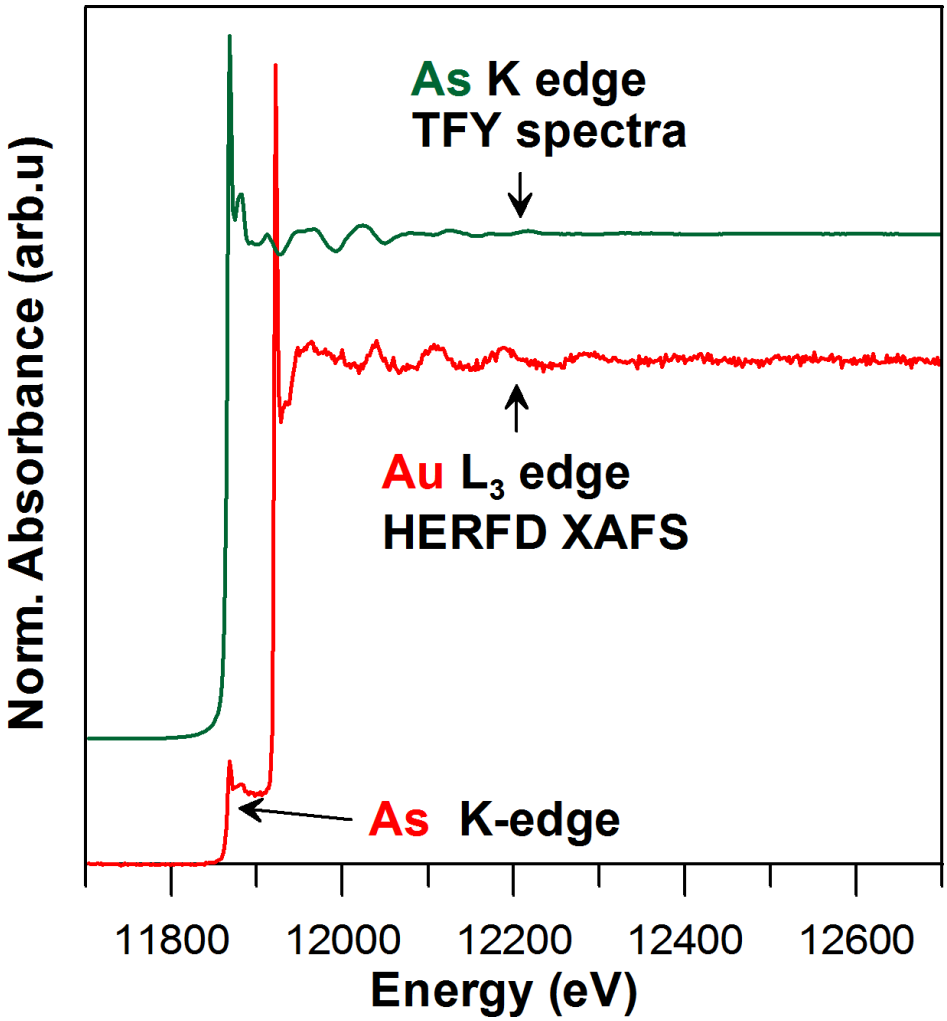
As K edge
TFY spectra
Au L3 edge
HERFD XAFS
As K-edge
Norm. Absorbance (arb.u)
11800
12000
12200
12400
12600
Energy (eV)

Fig. 2.

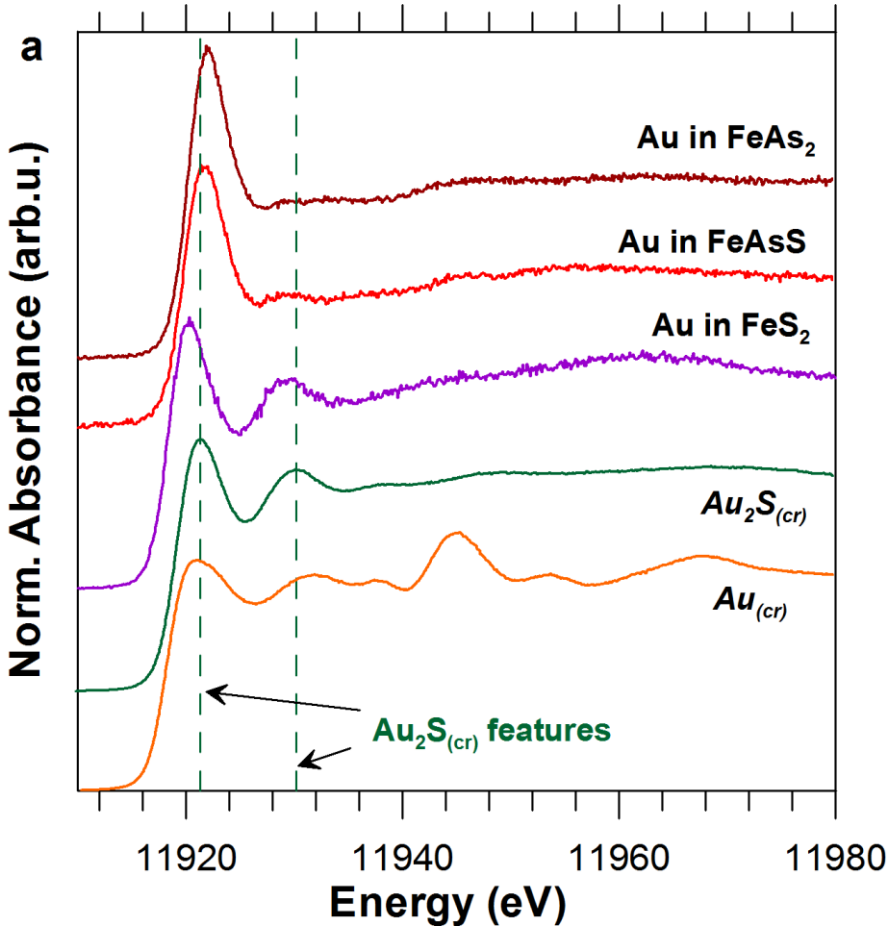
a
Norm. Absorbance (arb.u.)
Au in FeAs2
Au in FeAsS
Au in FeS2
Au2S(cr)
Au(cr)
Au2S(cr) features
11920
11940
11960
11980
Energy (eV)

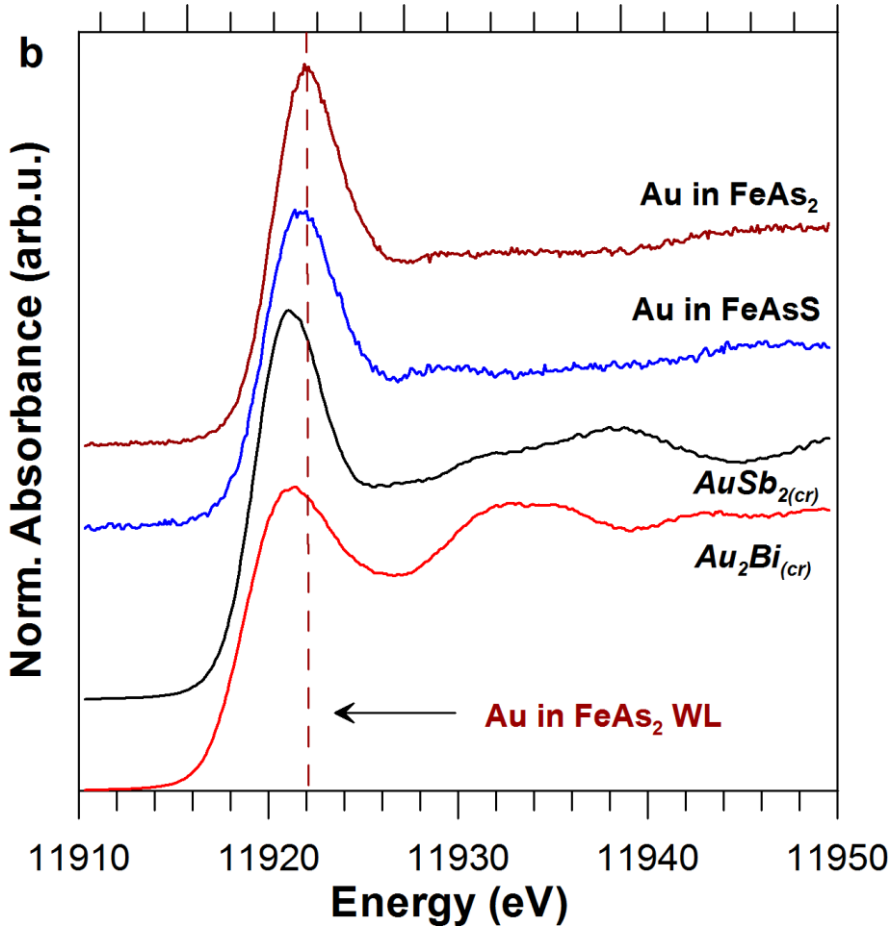
b
Norm. Absorbance (arb.u.)
Au in FeAs2
Au in FeAsS
AuSb2(cr)
Au2Bi(cr)
Au in FeAs2 WL
11910
11920
11930
11940
11950
Energy (eV)

Fig. 3.

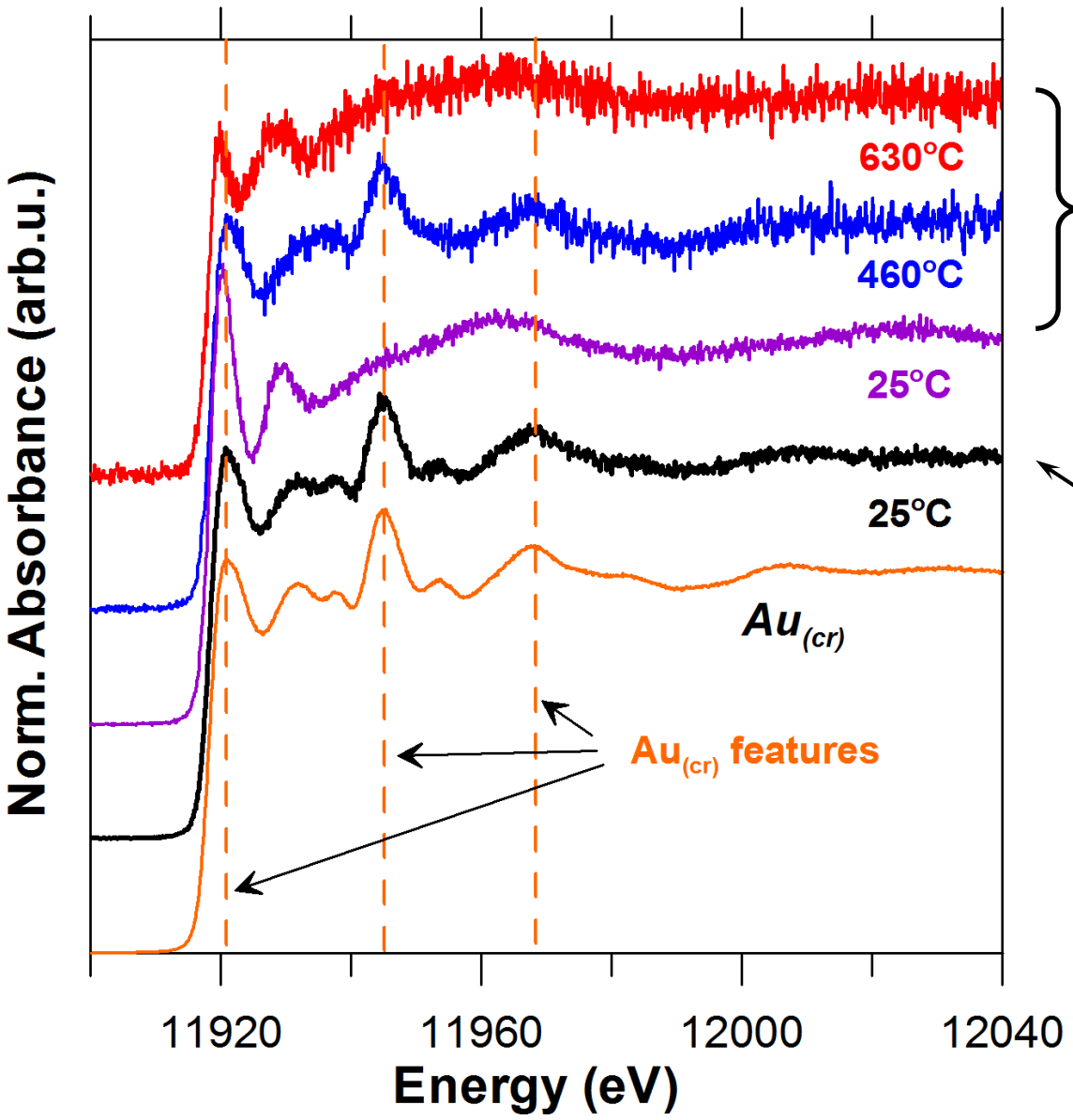

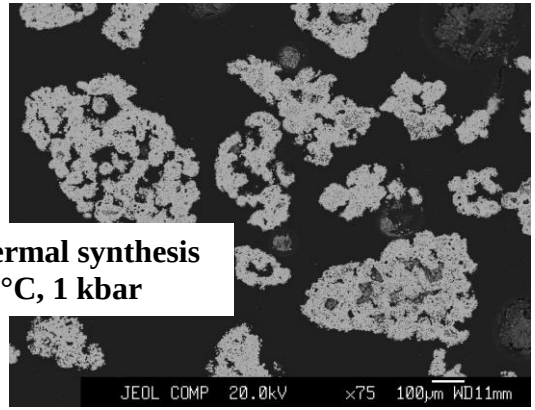

Hydrothermal synthesis
450 °C, 1 kbar

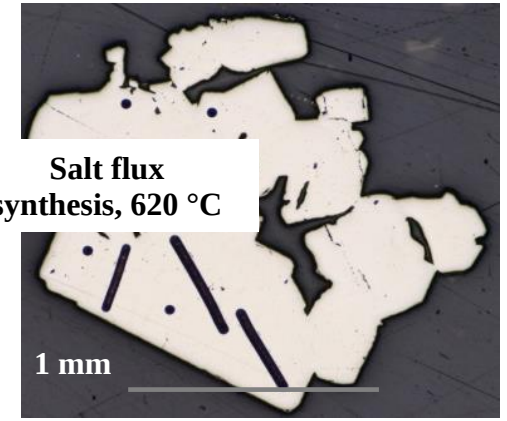

Salt flux
synthesis, 620 °C

Fig. 4

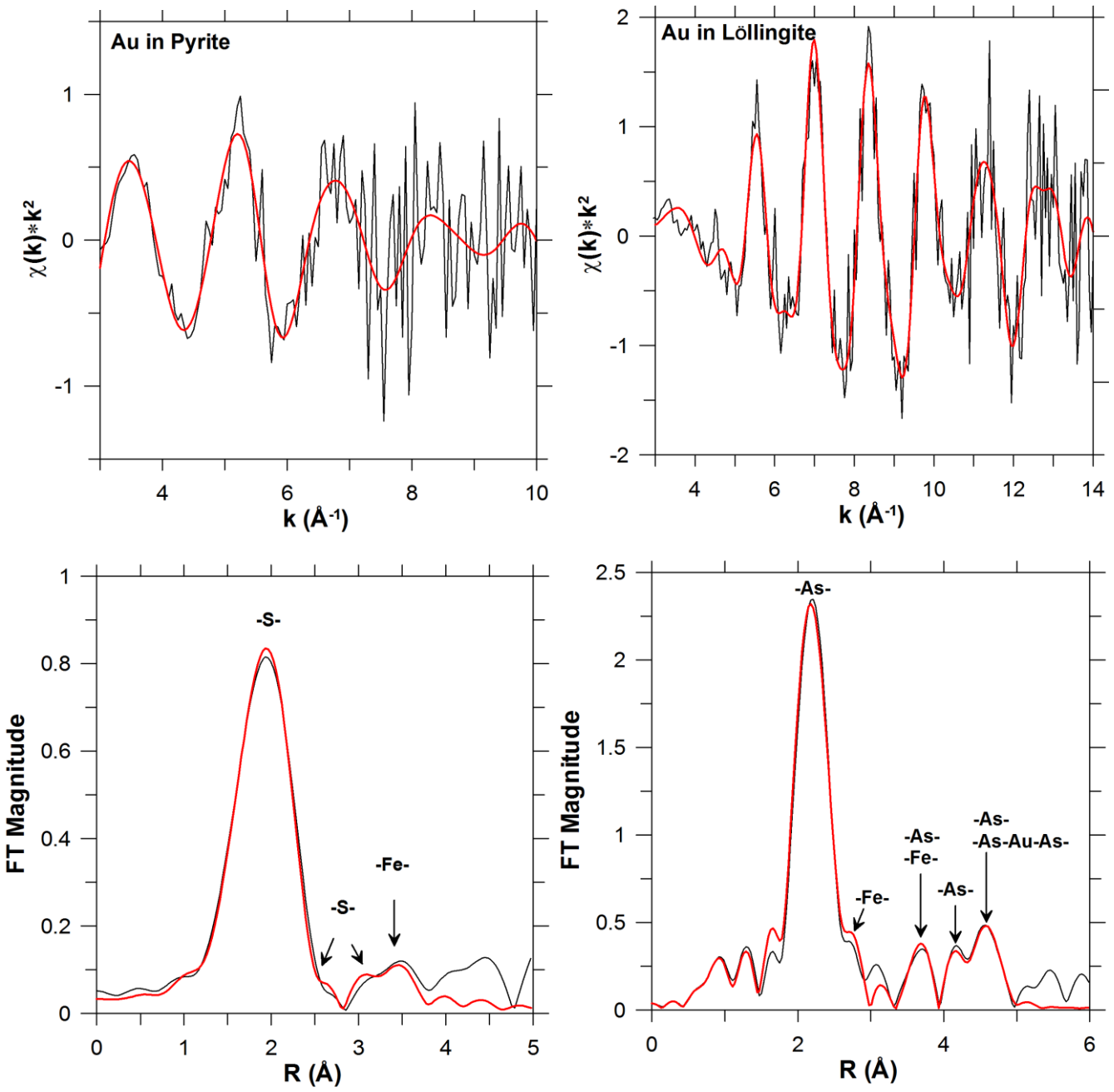
Au in Pyrite
χ(k)*k²
k (Å⁻¹)
Au in Löllingite
χ(k)*k²
k (Å⁻¹)
FT Magnitude
-S-
-S-
-Fe-
R (Å)
FT Magnitude
-As-
-Fe-
-As-
-Fe-
-As-
-As-Au-As-
R (Å)

Fig. 5

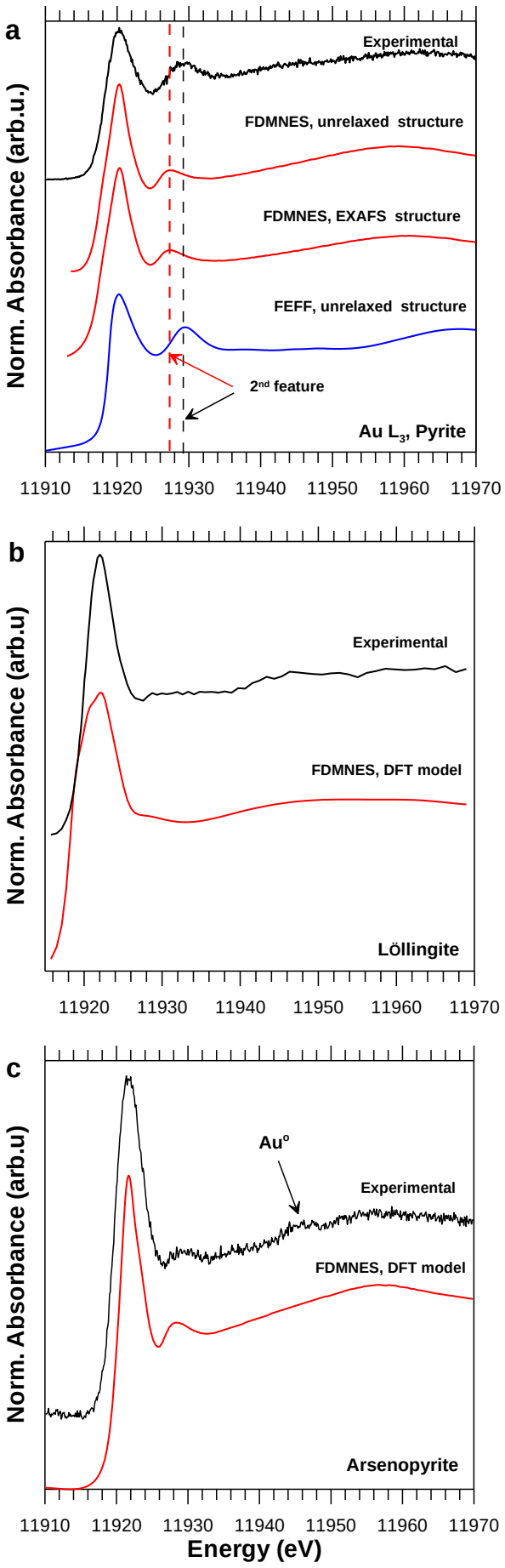
a
Norm. Absorbance (arb.u.)
Experimental
FDMNES, unrelaxed structure
FDMNES, EXAFS structure
FEFF, unrelaxed structure
2nd feature
Au L3, Pyrite
11910
11920
11930
11940
11950
11960
11970
b
Norm. Absorbance (arb.u)
Experimental
FDMNES, DFT model
Löllingite
11920
11930
11940
11950
11960
11970
c
Norm. Absorbance (arb.u)
Au°
Experimental
FDMNES, DFT model
Arsenopyrite
11910
11920
11930
11940
11950
11960
11970
Energy (eV)

Fig. 6